

Conditional Guided Generative Diffusion for Particle Accelerator Beam Diagnostics

Alexander Scheinker^{1,*}

¹Applied Electrodynamics Group, Los Alamos National Laboratory, Los Alamos, New Mexico, 87545, USA

*ascheink@lanl.gov

ABSTRACT

Advanced accelerator-based light sources such as free electron lasers (FEL) accelerate highly relativistic electron beams to generate incredibly short (10s of femtoseconds) coherent flashes of light for dynamic imaging, whose brightness exceeds that of traditional synchrotron-based light sources by orders of magnitude. FEL operation requires precise control of the shape and energy of the extremely short electron bunches whose characteristics directly translate into the properties of the produced light. Control of short intense beams is difficult due to beam characteristics drifting with time and complex collective effects such as space charge and coherent synchrotron radiation. Detailed diagnostics of beam properties are therefore essential for precise beam control. Such measurements typically rely on a destructive approach based on a combination of a transverse deflecting resonant cavity followed by a dipole magnet in order to measure a beam's 2D time vs energy longitudinal phase-space distribution. In this paper, we develop a non-invasive virtual diagnostic of an electron beam's longitudinal phase space at megapixel resolution (1024×1024) based on a generative conditional diffusion model. We demonstrate the model's generative ability on experimental data from the European X-ray FEL.

Introduction

Particle accelerators provide intense high energy charged particle beams for a wide range of scientific studies at otherwise inaccessible length, time, and energy scales. Free electron lasers (FEL) generate bright flashes of coherent light at femtosecond time scales which is incredibly useful for structural biology¹. FELs have been utilized for a wide range of biological studies including protein crystallography²⁻⁴, with a recent demonstration of single protein-based diffraction from a 14 nm diameter sample⁵. Two-color experiments with polarization control has enabled the use of FELs as tools for chiral recognition during photolysis⁶. FELs have been used to image viruses⁷, to study the structure and dynamics of macromolecules⁸, and FELs have been used to study matter in extreme conditions⁹. Utilizing FELs as femtosecond light sources has also enabled time-resolved site-specific investigations for understanding and benchmarking ultrafast photochemistry¹⁰. The data utilized in this work was collected at the European X-ray FEL (EuXFEL)¹¹. The EuXFEL is one of the most advanced FEL facilities in the world, capable of accelerating up to 5000 electron bunches per second up to energies of 17.5 GeV, with the FEL undulator producing hard X-rays at up to 14 keV with pulse energies of up to 2.0 mJ. The EuXFEL has been utilized for a wide range of scientific studies. Recent work at the EuXFEL includes the study of ribosome molecules¹², for developing crystal-based photon energy calibration techniques for FELs¹³, for the development of advanced single-particle X-ray diffractive imaging techniques¹⁴, for laser-driven dynamic compression experiments for fast formation of nanodiamonds¹⁵, for studies of ultrafast demagnetization induced by X-ray photons¹⁶, for the development of novel single X-ray pulse-based 3D atomic structure reconstructions¹⁷, and for ultrahigh resolution X-ray Thomson scattering¹⁸.

In FELs, photocathode properties are crucial as they define the initial conditions of the electron beams which are then accelerated and used to produce the FEL light. The improvement and development of advanced FEL photocathodes is a lively area of research including a wide range of studies on photocathode technology¹⁹⁻²³. Another area of intense FEL research is the development of non-destructive characterization methods for the FEL light pulses themselves. This is incredibly challenging as the pulses can be only 10s of femtoseconds in duration, but their characterization is crucial to fully understand the FEL-based imaging process and to verify the properties of the produced light. Towards these efforts, recently AI methods have been developed for online characterization of ultrashort X-ray free-electron laser pulses themselves²⁴.

After the electrons are produced at the photocathode and before they pass through the undulator to create intense pulses of light, the dynamics of intense electron bunches are influenced by complex collective effects such as wakefields, space charge, and coherent synchrotron radiation, making it difficult to control and tune beam properties using model-based approaches. Precisely shaping the 2D energy vs time longitudinal phase space distribution of the electron beam relies on an ability to measure that distribution in detail. The state of the art method for such measurements utilizes a x-band transverse deflecting cavity (XTCAV) to measure the beam. The XTCAV streaks the electron bunch, translating longitudinal position to transverse

position. The rotated bunch is passed through a vertical dipole causing an energy-dependent curvature of the electron trajectory, providing a measurement of both longitudinal bunch current profile and energy distribution²⁵. Several examples of such measurements taken at the European X-ray FEL (EuXFEL) are shown in Figure 1. The images shown are 1024×1024 pixels with a time resolution of 1.5 fs/pixel (because the electrons are traveling at near light speed that translates into 4.5 $\mu\text{m}/\text{pixel}$), the energy resolution is 20 keV/pixel, the bunch charge is 0.25 nC, and the bunch energy is 150 MeV.

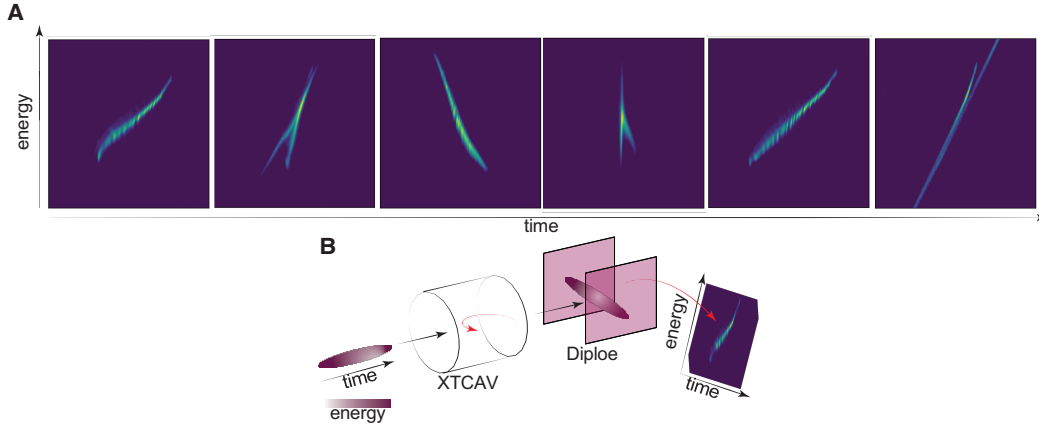


Figure 1. **A:** Examples of longitudinal phase space measurements of electron beam at the EuXFEL for various accelerator components settings. **B:** An overview of the destructive measurement process with the beam first rotated by a transverse deflecting RF cavity followed by energy-based dispersion of the beam with a dipole magnet.

The main limitation of a XTCAV-based measurement is that it is an invasive procedure which destroys the beam that is being measured and therefore that same beam cannot be accelerated further for experimental applications. Furthermore, in many facilities (such as the EuXFEL) choosing whether to send the beam off to a diagnostic section or to allow the beam to continue accelerating is a lengthy tuning procedure. It is not possible to simply switch back and forth at the push of a button. Therefore the initial accelerator section essentially runs at two different modes. First, the XTCAV diagnostics section is used for initial tuning, then the beam is only accelerated downstream without further use of the XTCAV.

It would be incredibly valuable to measure the detailed time vs energy distribution of the electron beam near the beginning of the accelerator at all times non-invasively, both to provide a detailed understanding of the electron beam's characteristics and also to use that information as input to online physics models which could then realistically estimate the beam's dynamics through subsequent accelerator sections. These days, various machine learning (ML)-based methods for particle accelerators, including for use as virtual diagnostics have been studied for many accelerator applications. For example, neural networks are being used for uncertainty aware anomaly detection to predict errant beam pulses²⁶.

In terms of virtual diagnostics, encoder-decoder neural networks were developed for the EuXFEL for generating longitudinal (z , E) phase-space images of the electron beam²⁷. Neural networks have been used to develop virtual diagnostics for 4D tomographic phase space reconstructions²⁸. Neural network-based methods have been developed for predicting the transverse emittance of space charge dominated beams²⁹. Adaptive neural networks using advanced feedback control algorithms³⁰ for adaptive latent space tuning of autoencoders have been developed to provide virtual 6D diagnostics of charged particle beams³¹, and these adaptive ML methods have been shown to increase the robustness of generative predictions far beyond the span of the training data, for tracking unknown time-varying beams³². Adaptive ML methods have also been designed for inverse problems that map downstream beam measurements back to the initial beam distribution³³. Recently, very interesting methods have also been studied for phase space reconstructions based on normalizing flows³⁴.

In this paper, the first diffusion based approach to non-invasive high resolution beam diagnostics is introduced. The diffusion-based model is developed for imaging the time vs energy longitudinal phase space distribution of a charged particle beam, and demonstrated on the European XFEL for accurately predicting the distributions of a diverse set of bunch profiles over a wide range of accelerator settings. Although this method is focused on a particle accelerator application, it is a very general approach, which can be used for any complex dynamic system for which it would be beneficial to replace invasive or destructive diagnostics of the system's state with virtual diagnostics which must rely on low-dimensional non-invasive measurements or parameter set points, as shown in Figure 2.

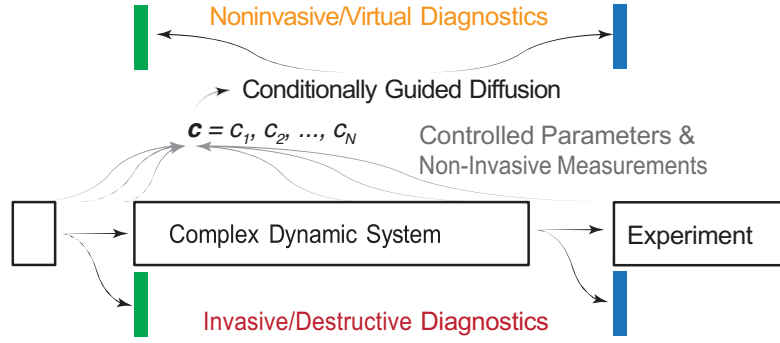


Figure 2. A general high-level overview of using conditional diffusion as a generative model that provides a non-destructive detailed view of the state of a complex system based on any available non-invasive diagnostics.

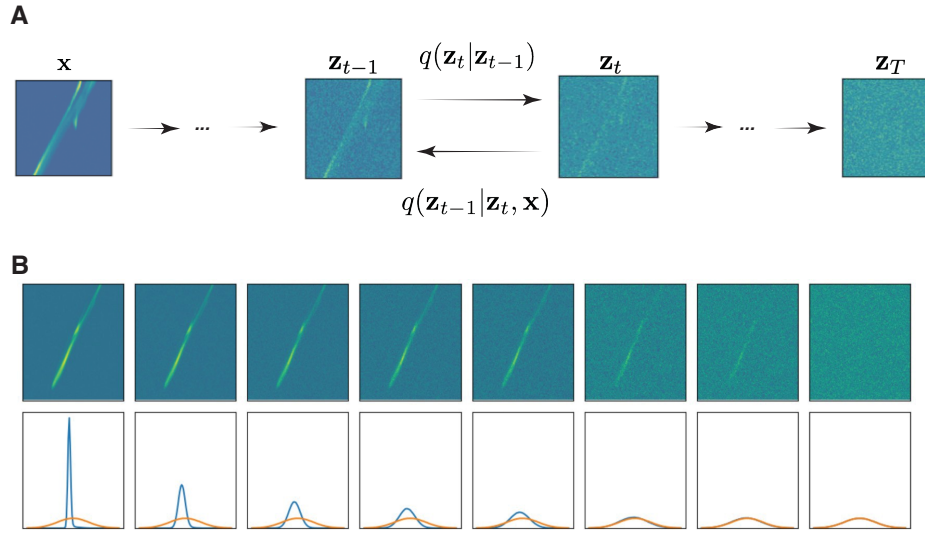


Figure 3. **A:** The forward diffusion process of a sample x is shown as it transforms to latent variables z_t which gradually approach a Gaussian distribution. **B:** A $T = 1000$ step diffusion process is shown at each 125 steps along with a histogram of the image pixel values at each step (blue) next to a mean zero unit variance Gaussian (yellow).

Methods

Generative models based on diffusion utilize a gradual denoising approach inspired by statistical thermodynamics for modeling complex distributions³⁵. This approach was then further developed for the generation of high resolution images^{36–39}. Diffusion-based generative models have now become the state-of-the-art for generating high resolution images, especially when the images have a wide variety. The generative ability of diffusion-based models has made them powerful tools for a wide range of scientific applications⁴⁰, such as conditional generation of hypothetical new families of superconductors⁴¹, for brain imaging⁴², for various bioengineering applications⁴³, for protein structure generation⁴⁴.

The diffusion-based method used in this work is based on a modified version of the approach described in³⁶. In our approach we add an additional conditional input vector along with the time embedding to perform guided diffusion which maps specific accelerator conditions to beam images. For completeness, we briefly outline the generative diffusion theory and refer readers to³⁶ for details and proofs.

The generative diffusion process works by adding noise to an image x over a large number of steps T until the pixel values of the image closely resemble a mean zero unit variance Gaussian distribution as shown in the left to right flow of Figure 3.

For an image x , the first step of the diffusion process is to create a noise-corrupted image z_1 as defined by

$$z_1 = \sqrt{1 - \beta_1}x + \sqrt{\beta_1}\epsilon_1, \quad \epsilon_1 \sim \mathcal{N}(\epsilon_1 | 0, I)(1)$$

with subsequent diffusion steps iteratively defined as

$$z_t = \sqrt{1 - \beta_t} z_{t-1} + \sqrt{\beta_t} \epsilon_t, \quad \epsilon_t \sim \mathcal{N}(\epsilon_t | 0, I), \quad t \in \{2, \dots, T\} \quad (2)$$

The noise schedule $\beta_t \in [0, 1]$ with $\beta_1 < \beta_2 < \dots < \beta_T$ prescribes the variance for the additive unit variance Gaussian noise ϵ_t at each step t which defines how quickly images are converted to pure noise. This diffusion sequence forms a Markov chain with conditional distributions of the form

$$q(z_t | z_{t-1}) = \mathcal{N}(z_t | \sqrt{1 - \beta_t} z_{t-1}, \beta_t I), \quad (3)$$

which is convenient for sampling random diffusion steps t without having to re-run the entire chain as z_t can be rewritten as

$$z_t = \sqrt{\alpha_t} x + \sqrt{1 - \alpha_t} \epsilon_t \quad (4)$$

where $\sqrt{1 - \alpha_t} \epsilon_t$ represents the total noise added to the original image and α_t is the product.

$$\alpha_t = \prod_{\tau=1}^t (1 - \beta_\tau) \quad (5)$$

Equation (4) implies that

$$q(z_t | x) = \mathcal{N}(z_t | \sqrt{\alpha_t} x, (1 - \alpha_t) I), \quad (6)$$

and therefore, since $(1 - \beta_t) < 1$, as $T \rightarrow \infty$ the terms α_t and $1 - \alpha_t$ approach 0 and 1, respectively, and

$$\lim_{T \rightarrow \infty} q(z_T | x) = \mathcal{N}(z_T | 0, I), \quad (7)$$

which means that any image is converted to a signal indistinguishable from mean 0 unit variance Gaussian noise. In practice values such as $T = 1000$ are a good choice, which is also the number of diffusion steps used in this work. The noise schedule is chosen with endpoints as in³⁶ with β_t increasing linearly from 10^{-4} to 0.02 over $T = 1000$ steps. While nonlinear noise schedules were proposed in³⁸, the authors pointed out that they were mostly beneficial for lower resolution images, and that was confirmed in this work as a cosine noise schedule performed similarly to the linear one.

In order to generate images, the model must learn to run backwards, undoing the diffusion process. For a given image x , Baye's rule and the Gaussian change of variables identity allow us to write the conditional probability $q(z_{t-1} | z_t, x)$ which describes one reverse step of the diffusion process, as:

$$q(z_{t-1} | z_t, x) = \mathcal{N}\left(z_{t-1} \left| \frac{1 - \alpha_{t-1}}{1 - \alpha_t} \sqrt{1 - \beta_t} z_t + \frac{\sqrt{\alpha_{t-1} \beta_t}}{1 - \alpha_t} x, \frac{\beta_t (1 - \alpha_{t-1})}{1 - \alpha_t} I \right.\right). \quad (8)$$

By rewriting Equation (4) as _____

$$x = \frac{1}{\sqrt{1 - \beta_t}} z_t - \frac{\sqrt{\beta_t}}{\sqrt{1 - \beta_t}} \epsilon_t, \quad (9)$$

and plugging that into the mean value of the prediction in Equation 8, the model can be effectively used to predict how to remove noise between iterative steps to restore the original image according to

$$z_{t-1} = \frac{1}{\sqrt{1 - \beta_t}} \left[z_t - \frac{\beta_t}{\sqrt{1 - \alpha_t}} D(z_t, t, c) \right] + \sqrt{\beta_t} \epsilon, \quad \epsilon \sim \mathcal{N}(\epsilon | 0, I). \quad (10)$$

At the final generation step, the image is created according to

$$x = \frac{1}{\sqrt{1 - \beta_1}} \left[z_1 - \frac{\beta_1}{\sqrt{1 - \alpha_1}} D(z_1, t, c) \right]. \quad (11)$$

One example of such diffusion-based image generation is shown in Figure 4.



Figure 4. From left to right the first ten images show diffusion steps 100, 200, ..., 1000 followed by the true target image and finally the difference between the two.

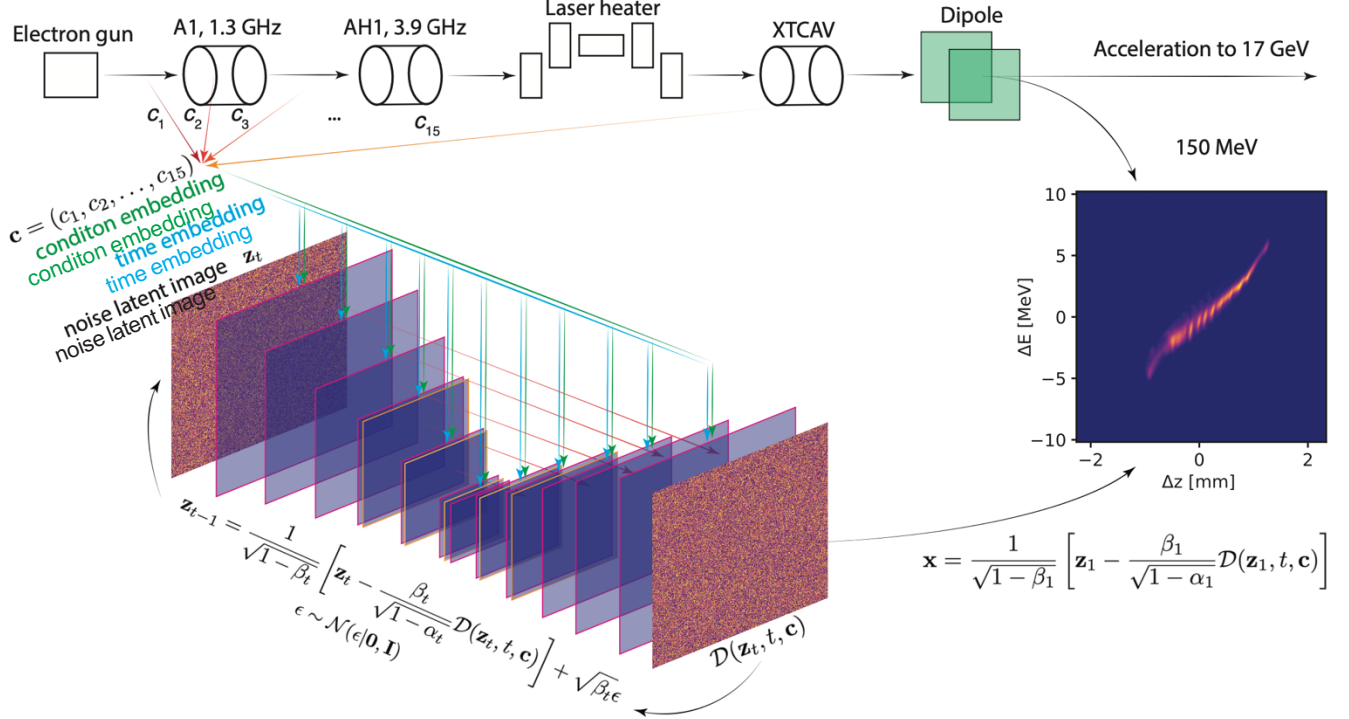


Figure 5. Conditional diffusion setup for generating XTCAV images of the beam's (z, E) longitudinal phase space projection.

Results

This work demonstrates that a conditionally guided generative diffusion process can be used to accurately generate unseen test data to give a non-invasive virtual high resolution view of the electron beam's longitudinal (z, E) phase at the EuXFEL. In this approach, the conditional input vector is $\mathbf{c} \in \mathbb{R}^{15}$ utilizing 5 accelerator parameter set points and 10 non-invasive beam-based measurements, as shown in Figure 5. The first 5 parameters of \mathbf{c} are settings of three energy chirps (energy vs time correlations) imposed by radio frequency (RF) resonant cavity fields onto the electron beam as it passes from the electron gun through the A1 and AH1 sections of the accelerator. The curvature of this chirp is also controlled and so is the third derivative by using 3.9 GHz RF which is at the third harmonic of the EuXFEL's overall 1.3 GHz RF system. The remaining 10 parameters are RMS X and Y beam centroid values measured at 5 locations between the injector and the XTCAV. The data used for this work was gathered at the EuXFEL by varying the first 5 parameters above randomly within a wide range. From 11000 data points, 10000 were used for training and 1000 for testing.

This generative conditionally guided diffusion approach results in an ability to create incredibly high resolution megapixel beam images for a very wide range of beams, which is exactly the application for which diffusion-based models are state-of-the-art. Figure 7 shows three detailed examples of very different very complex beams generated by the conditional diffusion process next to the true images.

To quantify the reconstruction accuracy the absolute percent error was calculated between generated images \hat{Y} and their true measurements Y according to

$$E = 100 \times \sum_i \sum_j |Y - \hat{Y}| / \sum_i \sum_j |Y|, \quad (12)$$

where $i, j \in \{1, 1024\}$ are the pixel locations within the images. Figure 6 quantitatively shows the generative error as defined in

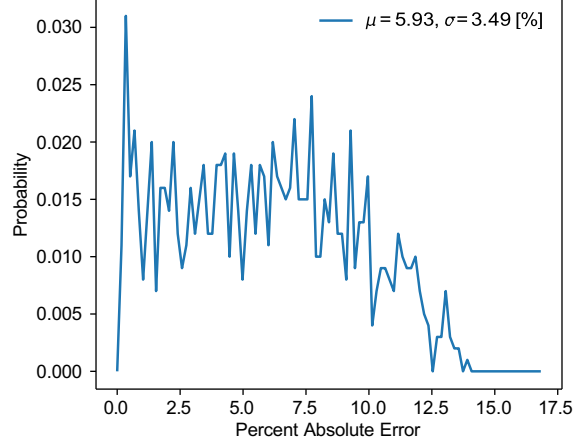


Figure 6. Error statistics for 1000 test images. The overall mean absolute percent error was 5.93 % with a standard deviation of 3.49 %.

Equation 12 for 1000 unseen test objects. For a visualization of how these error levels correspond to image quality, Figure 8 shows 5 examples from the test data set, of increasing error. It can be seen that up to $\sim 10\%$ error the predictions are very accurate.

These results demonstrate that the conditionally guided diffusion model can serve as a highly accurate virtual diagnostic of the electron beam’s longitudinal phase space for a wide range of accelerator settings, without having to intercept and destroy the beam to measure it.

Moving Along the Image Manifold by Latent Space Interpolation

Once the diffusion model has been trained to generate a electron beam images associated with a wide range of accelerator settings, it is possible to smoothly move between various accelerator setups while generating realistic electron bunch distributions. Given two different accelerator setups ($\mathbf{c}_0, \mathbf{c}_1$) and their associated electron beam images ($\mathbf{x}_0, \mathbf{x}_1$), it would be useful to understand how the beam behaves at an intermediate state between these two. One simple naive way to attempt to approximate this is a linear interpolation between the two images of the form

$$\mathbf{x}_t = (1-t)\mathbf{x}_0 + t\mathbf{x}_1, \quad t \in [0, 1], \quad t : 0 \rightarrow 1 \quad \Rightarrow \quad \mathbf{x}_t : \mathbf{x}_0 \rightarrow \mathbf{x}_1. \quad (13)$$

This method results in a non-physical weighted superposition of the two images, as shown on the left side of Figure 9.

The trained diffusion model allows us to move between accelerator settings in a more physical way, as the network utilizes all of the training data in order to interpolate in a physically consistent way. In this approach, for the two images ($\mathbf{x}_0, \mathbf{x}_1$) we first perform a conditional generation of the two images based on two random noise images ($\mathbf{n}_0, \mathbf{n}_1$) and on their two conditioning vectors which correspond to accelerator settings ($\mathbf{c}_0, \mathbf{c}_1$). Together we treat the noise-vector pairs as latent variables ($\mathbf{z}_0, \mathbf{z}_1$). We now perform the same linear interpolation as above, but in the latent space directly according to

$$\mathbf{z}_t = (1-t)\mathbf{z}_0 + t\mathbf{z}_1, \quad t \in [0, 1], \quad t : 0 \rightarrow 1 \quad \Rightarrow \quad \mathbf{z}_t : \mathbf{z}_0 \rightarrow \mathbf{z}_1. \quad (14)$$

At each time step along the latent path \mathbf{z}_t we can then perform conditional generation via the learned diffusion process in order to generate an image \mathbf{x}_t which is no longer a simple superposition of the two images, but rather is a true intermediate state that is moving along the learned image manifold

$$\mathbf{x}_t = D(\mathbf{z}_t) = D((1-t)\mathbf{z}_0 + t\mathbf{z}_1), \quad (15)$$

as shown on the right side of Figure 9.

Discussion

This paper has demonstrated that conditionally guided generative diffusion models can be utilized as high resolution virtual diagnostics for charged particle beams. It was shown that the models can make accurate predictions for unseen test data within a very diverse set of measurements, and that the trained models can be used to smoothly traverse the learned latent embedding in

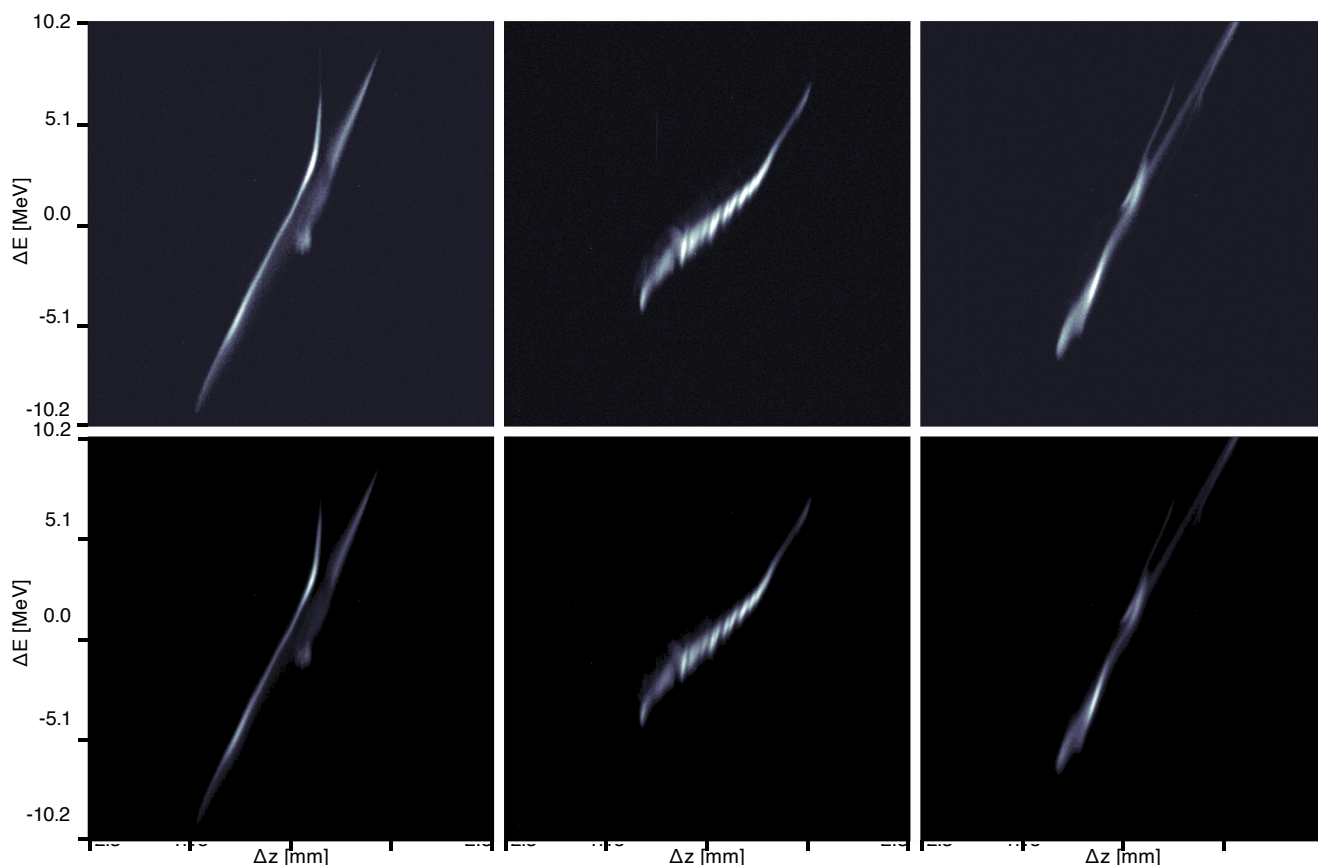


Figure 7. The top row shows a detailed view of 3 conditionally generated electron beam images at 1024 \times 1024 pixel resolution, based on a 1000-step diffusion process. The bottom row shows the target electron beam images.

order to interpolate between various accelerator settings in a physical way. Although this work was focused on high resolution 2D (z , E) longitudinal phase space predictions, because those are some of the most important measurements for FEL operations, this same approach can be used to model any of the beam's projections, including all of the 15 unique 2D projections of a beam's 6D phase space as was already done with autoencoder-based generative models^{31,32}. The benefit of using diffusion for this approach should be in generating higher resolution images.

Beyond particle accelerators, such a conditionally guided diffusion process could be very useful for any complex dynamic system in which it would be beneficial to replace a destructive / invasive diagnostic of the system state with a virtual non-invasive virtual diagnostic.

References

1. Nakagawa, A., Helliwell, J. R. & Yamagata, Y. Diffraction structural biology—an introductory overview. *Acta Crystallogr. Sect. D: Struct. Biol.* **77**, 278–279 (2021).
2. Koopmann, R. *et al.* In vivo protein crystallization opens new routes in structural biology. *Nat. methods* **9**, 259–262 (2012).
3. Chapman, H. N. *et al.* Femtosecond x-ray protein nanocrystallography. *Nature* **470**, 73–77 (2011).
4. Johansson, L. C. *et al.* Lipidic phase membrane protein serial femtosecond crystallography. *Nat. methods* **9**, 263–265 (2012).
5. Ekeberg, T. *et al.* Observation of a single protein by ultrafast x-ray diffraction. *Light. Sci. & Appl.* **13**, 15 (2024).
6. Ilchen, M. *et al.* Site-specific interrogation of an ionic chiral fragment during photolysis using an x-ray free-electron laser. *Commun. Chem.* **4**, 119 (2021).
7. Munke, A. *et al.* Coherent diffraction of single rice dwarf virus particles using hard x-rays at the linac coherent light source. *Sci. data* **3**, 1–12 (2016).

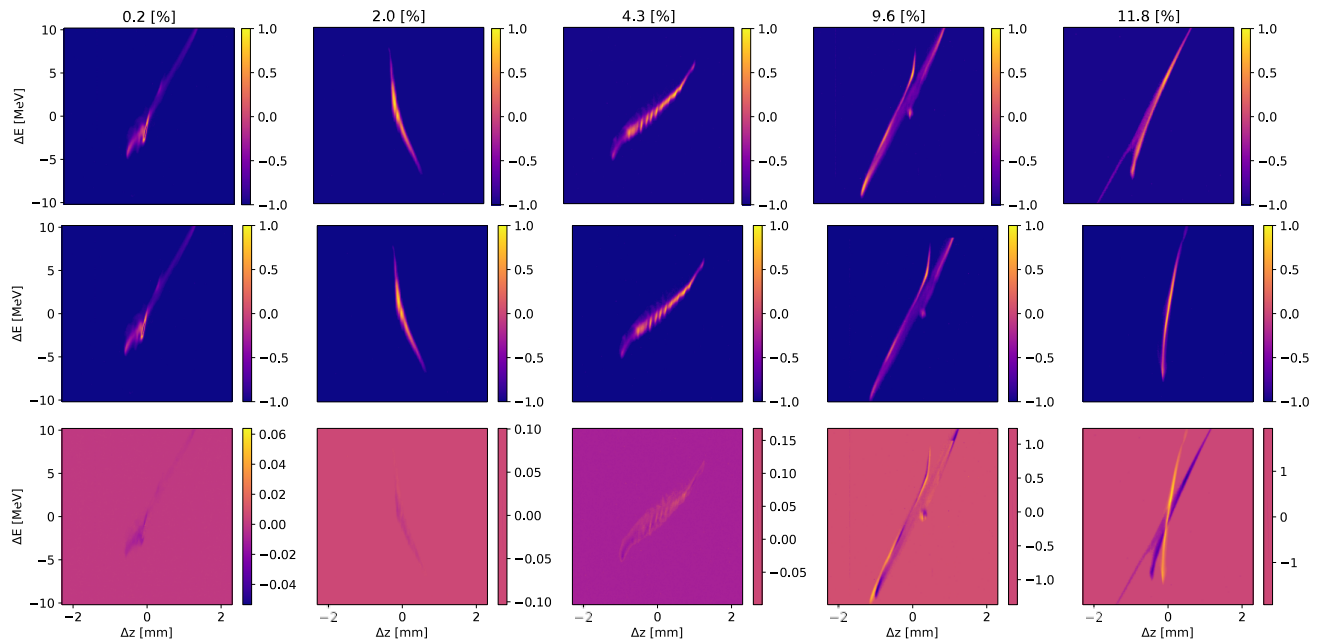


Figure 8. Detailed view of 5 reconstructed test images of increasing percent absolute error from left to right.

8. Chapman, H. N. X-ray free-electron lasers for the structure and dynamics of macromolecules. *Annu. review biochemistry* **88**, 35–58 (2019).
9. Vinko, S. *et al.* Creation and diagnosis of a solid-density plasma with an x-ray free-electron laser. *Nature* **482**, 59–62 (2012).
10. Allum, F. *et al.* A localized view on molecular dissociation via electron-ion partial covariance. *Commun. Chem.* **5**, 42 (2022).
11. Decking, A. S. A. P. e. a., W. A MHz-repetition-rate hard X-ray free-electron laser driven by a superconducting linear accelerator. *Nat. Photonics* **14**, 391–397, DOI: [10.1038/s41566-020-0607-z](https://doi.org/10.1038/s41566-020-0607-z) (2020).
12. Stransky, M. *et al.* Computational study of diffraction image formation from xfel irradiated single ribosome molecule. *Sci. reports* **14**, 10617 (2024).
13. Grech, C. *et al.* Crystal-based absolute photon energy calibration methods for hard x-ray free-electron lasers. *Phys. Rev. Accel. Beams* **27**, 050701 (2024).
14. Yenupuri, T. V. *et al.* Helium-electrospray improves sample delivery in x-ray single-particle imaging experiments. *Sci. Reports* **14**, 4401 (2024).
15. Heuser, B. *et al.* Release dynamics of nanodiamonds created by laser-driven shock-compression of polyethylene terephthalate. *Sci. Reports* **14**, 12239 (2024).
16. Kaptcia, K. J. *et al.* Ultrafast demagnetization in bulk nickel induced by x-ray photons tuned to ni m 3 and l 3 absorption edges. *Sci. Reports* **14**, 473 (2024).
17. Bortel, G. *et al.* 3d atomic structure from a single x-ray free electron laser pulse. *Nat. Commun.* **15**, 970 (2024).
18. Gawne, T. *et al.* Ultrahigh resolution x-ray thomson scattering measurements at the european x-ray free electron laser. *Phys. Rev. B* **109**, L241112 (2024).
19. Moody, N. A. *et al.* Perspectives on designer photocathodes for x-ray free-electron lasers: Influencing emission properties with heterostructures and nanoengineered electronic states. *Phys. Rev. Appl.* **10**, 047002 (2018).
20. Yamaguchi, H. *et al.* Quantum efficiency enhancement of bialkali photocathodes by an atomically thin layer on substrates. *physica status solidi (a)* **216**, 1900501 (2019).
21. Wang, E. *et al.* Long lifetime of bialkali photocathodes operating in high gradient superconducting radio frequency gun. *Sci. Reports* **11**, 4477 (2021).

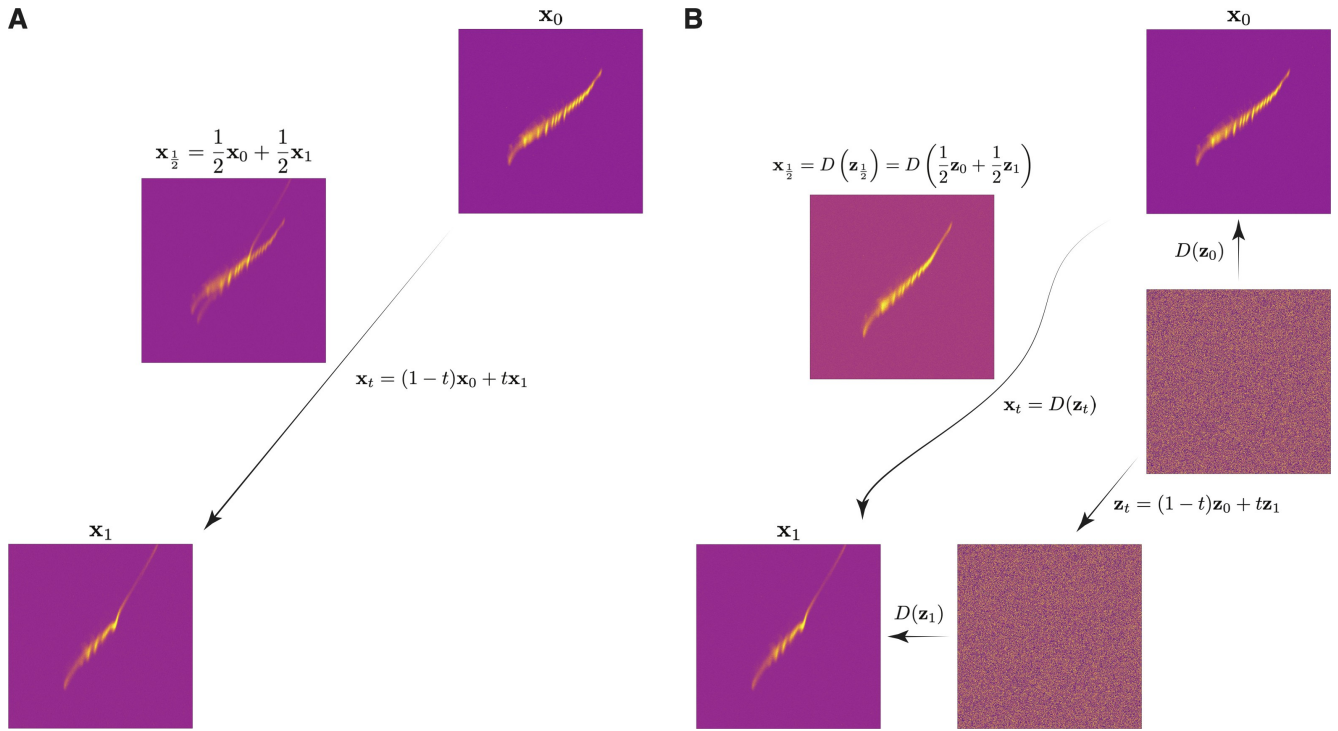


Figure 9. Left: Performing a simple linear interpolation between two images of the electron beam (x_0, x_1) at two different accelerator settings results. Right: Performing linear interpolation in the latent space.

22. Yamaguchi, H. *et al.* Work function lowering of lab6 by monolayer hexagonal boron nitride coating for improved photo-and thermionic-cathodes. *Appl. Phys. Lett.* **122** (2023).
23. Knill, C. J. *et al.* Near-threshold photoemission from graphene-coated cu (110). *Phys. Rev. Appl.* **19**, 014015 (2023).
24. Dingel, K. *et al.* Artificial intelligence for online characterization of ultrashort x-ray free-electron laser pulses. *Sci. Reports* **12**, 17809 (2022).
25. Behrens, C. *et al.* Few-femtosecond time-resolved measurements of x-ray free-electron lasers. *Nat. communications* **5**, 3762 (2014).
26. Blokland, W. *et al.* Uncertainty aware anomaly detection to predict errant beam pulses in the oak ridge spallation neutron source accelerator. *Phys. Rev. Accel. Beams* **25**, 122802 (2022).
27. Zhu, J. *et al.* High-fidelity prediction of megapixel longitudinal phase-space images of electron beams using encoder-decoder neural networks. *Phys. Rev. Appl.* **16**, 024005 (2021).
28. Wolski, A., Johnson, M. A., King, M., Militsyn, B. L. & Williams, P. H. Transverse phase space tomography in an accelerator test facility using image compression and machine learning. *Phys. Rev. Accel. Beams* **25**, 122803 (2022).
29. Mayet, F. *et al.* Predicting the transverse emittance of space charge dominated beams using the phase advance scan technique and a fully connected neural network. *Phys. Rev. Accel. Beams* **25**, 094601 (2022).
30. Scheinker, A. & Krstic', M. Minimum-seeking for clfs: Universal semiglobally stabilizing feedback under unknown control directions. *IEEE Transactions on Autom. Control.* **58**, 1107–1122 (2012).
31. Scheinker, A. Adaptive machine learning for time-varying systems: low dimensional latent space tuning. *J. Instrumentation* **16**, P10008 (2021).
32. Scheinker, A., Cropp, F. & Filippetto, D. Adaptive autoencoder latent space tuning for more robust machine learning beyond the training set for six-dimensional phase space diagnostics of a time-varying ultrafast electron-diffraction compact accelerator. *Phys. Rev. E* **107**, 045302 (2023).
33. Scheinker, A., Cropp, F., Paigua, S. & Filippetto, D. An adaptive approach to machine learning for compact particle accelerators. *Sci. reports* **11**, 19187 (2021).

34. Hoover, A. & Wong, J. C. High-dimensional maximum-entropy phase space tomography using normalizing flows. *arXiv preprint arXiv:2406.00236* (2024).
35. Sohl-Dickstein, J., Weiss, E., Maheswaranathan, N. & Ganguli, S. Deep unsupervised learning using nonequilibrium thermodynamics. In *International conference on machine learning*, 2256–2265 (PMLR, 2015).
36. Ho, J., Jain, A. & Abbeel, P. Denoising diffusion probabilistic models. *Adv. neural information processing systems* **33**, 6840–6851 (2020).
37. Song, J., Meng, C. & Ermon, S. Denoising diffusion implicit models. *arXiv preprint arXiv:2010.02502* (2020).
38. Nichol, A. Q. & Dhariwal, P. Improved denoising diffusion probabilistic models. In *International conference on machine learning*, 8162–8171 (PMLR, 2021).
39. Karras, T., Aittala, M., Aila, T. & Laine, S. Elucidating the design space of diffusion-based generative models. *Adv. neural information processing systems* **35**, 26565–26577 (2022).
40. Yang, L. *et al.* Diffusion models: A comprehensive survey of methods and applications. *ACM Comput. Surv.* **56**, 1–39 (2023).
41. Yuan, S. & Dordevic, S. Diffusion models for conditional generation of hypothetical new families of superconductors. *Sci. Reports* **14**, 10275 (2024).
42. Pinaya, W. H. *et al.* Brain imaging generation with latent diffusion models. In *MICCAI Workshop on Deep Generative Models*, 117–126 (Springer, 2022).
43. Guo, Z. *et al.* Diffusion models in bioinformatics and computational biology. *Nat. reviews bioengineering* **2**, 136–154 (2024).
44. Wu, K. E. *et al.* Protein structure generation via folding diffusion. *Nat. communications* **15**, 1059 (2024).

Acknowledgements

This work was supported by the U.S. Department of Energy (DOE), Office of Science, Office of High Energy Physics and the Los Alamos National Laboratory LDRD Program Directed Research (DR) project 20220074DR. This research used resources provided by the Los Alamos National Laboratory Institutional Computing Program, which is supported by the U.S. Department of Energy National Nuclear Security Administration under Contract No. 89233218CNA000001.

Competing interests

The author declares no competing interests.